A multi-stem cell basis for craniosynostosis and calvarial mineralization

Matthew Greenblatt (✉ mag3003@med.cornell.edu)

Weill Cornell Medicine and Hospital for Special Surgery   https://orcid.org/0000-0001-9794-8532

Seoyeon Bok

Weill Cornell Medicine, Cornell University   https://orcid.org/0000-0001-6063-1224

Alisha Yallowitz

Cornell University

Jason McCormick

Weill Cornell Medicine, Cornell University

Michelle Cung

Weill Cornell Medicine, Cornell University

Jun Sun

Weill Cornell Medicine, Cornell University

Sarfaraz Lalani

Weill Cornell Medicine, Cornell University

Zan Li

Weill Cornell Medicine, Cornell University

Tomas Baumgartner

Weill Cornell Medicine, Cornell University

Paul Byrne

Weill Cornell Medicine, Cornell University

Branden Sosa

Weill Cornell Medicine, Cornell University

Tuo Zhang

Weill Cornell Medical College   https://orcid.org/0000-0001-5396-918X

Fatma Mohamed

University of Michigan School of Dentistry

Chunxi Ge

University of Michigan School of Dentistry

Renny Franceschi

University of Michigan School of Dentistry

Randy Cowling

University of California-San Diego

Barry Greenberg

University of California-San Diego

David Pisapia

Weill Cornell Medicine   https://orcid.org/0000-0003-1528-8425

Thomas Imahiyerobo Jr

New York-Presbyterian Hospital/Columbia University Medical Center

Shenela Lakhani

Weill Cornell Medicine

Margaret Ross

Weill Cornell Medicine   https://orcid.org/0000-0001-6440-8089

Caitlin Hoffman

Weill Cornell Medicine

Shawon Debnath

Weill Cornell Medicine

Biological Sciences - Article

Keywords: Stem cell, Bone, Craniosynostosis, Calvarium

Abstract

Craniosynostosis is a group of disorders of premature calvarial sutural fusion. An incomplete understanding of the calvarial stem cells (CSCs) that produce fusion-driving osteoblasts has limited the development of non-surgical therapeutic approaches for craniosynostosis. Here we show that both physiologic calvarial mineralization and pathologic calvarial fusion in craniosynostosis reflect the interaction of two separate stem cell lineages; a recently reported CathepsinK (CTSK) lineage CSC (CTSK+ CSC)1 and a separate Discoidin domain-containing receptor 2 (DDR2) lineage stem cell (DDR2+ CSC) identified in this study. Deletion of Twist1, a gene associated with human craniosynostosis2,3, solely in CTSK+ CSCs is sufficient to drive craniosynostosis, however the sites destined to fuse surprisingly display a marked depletion of CTSK+ CSCs and a corresponding expansion of DDR2+ CSCs. This DDR2+ CSC expansion is a direct maladaptive response to CTSK+ CSC depletion, as partial suture fusion occurred after genetic ablation of CTSK+ CSCs. This DDR2+ CSC is a specific fraction of DDR2+ lineage cells that displayed full stemness features, establishing the presence of two distinct stem cell lineages in the sutures, with each population contributing to physiologic calvarial mineralization. DDR2+ CSCs mediate a distinct form of endochondral ossification where an initial cartilage template is formed but the recruitment of hematopoietic marrow is absent. Direct implantation of DDR2+ CSCs into suture sites was sufficient to induce fusion, and this phenotype was prevented by co-transplantation of CTSK+ CSCs. Lastly, the human counterparts of DDR2+ CSCs and CTSK+ CSCs are present in calvarial surgical specimens and display conserved functional properties in xenograft assays. The interaction between these two stem cell populations provides a new biologic interface to modulate calvarial mineralization and suture patency.

Main Text

Given that CTSK^{+} CSCs (sutural Lin^{-}/Thy-1.2^{-}/6C3^{-}/CD200^{+}/CD105^{-} calvarial stem cells expressing a *Ctsk-Cre* driven lineage reporter) contribute to physiologic calvarial mineralization[1], we hypothesized that defects in these cells may underlie calvarial disorders such as craniosynostosis. To examine this, we generated mice with a *Ctsk-Cre* driven conditional deletion of *Twist1* (*Twist1[Ctsk]*), as TWIST1 loss of function causes one of the most common craniosynostosis disorders, Saethre-Chotzen Syndrome[2,3]. Indeed, deletion of *Twist1* in CTSK^{+} lineage cells was sufficient to drive the suture fusion phenotype associated with this disorder, including fusion of the coronal (COR), lambdoid (LAM), squamosal (SQ), and occipitointerparietal (OIP) sutures (Fig. 1a, b, Extended Data Fig. 1a). While we expected expansion and activation of CTSK[+] CSCs to mediate fusion, we surprisingly instead observed a marked depletion of CTSK^{+} cells at the sutures destined to fuse and noted a correspondence between the degree of depletion and the completeness of fusion at each suture (Fig. 1c, Extended Data Fig. 1b, c). At these sites, CTSK[+] CSCs and their derivatives were replaced with another cell type not bearing the CTSK-lineage reporter (Fig. 1d, Extended Data Fig. 1d).

This dropout of CTSK[+] CSCs was accompanied by a major shift in the form of bone formation in the sutures.   Previously, we reported that CTSK[+] CSCs are specialized for the major physiologic form of calvarial bone formation, intramembranous bone formation[1], where bone is deposited directly without a cartilage template. Accordingly, dropout of CTSK[+] CSCs was accompanied by the pathologic induction of endochondral bone formation, where a cartilage template precedes mineralization, a form of bone formation normally excluded from the sutures[4−6] (Fig. 1e). Cartilage clusters were observed in the sutures destined to fuse, but this cartilage was fully remodeled into the bone at later timepoints, distinguishing this endochondral ossification process from the formation of ectopic cartilage (Fig. 1b, Extended Data Fig. 1e). Taken together, this data pointed to the existence of a second calvarial lineage distinct from CTSK^{+} lineage cells where these non-CTSK (CTSK^{-}) lineage cells emerge to become the dominant cell type in the sutures during fusion and are associated with endochondral bone formation.

Dropout of CTSK[+] CSCs was sufficient to drive the expansion of this alternative CTSK[-] population and suture fusion, as seen with inducible deletion of CTSK[+] CSCs using diphtheria toxin (DT) administration in *iDTR;Ctsk-Cre* (*iDTR[Ctsk]*) mice. These mice not only displayed hypomineralization of the calvarium similar to that seen after conditionally deleting the *Osterix* (*Osx*) gene required for osteoblast generation in CTSK^{+} cells (*Osx[Ctsk]*)[1], but also displayed partial suture fusion at similar sites to those fused in *Twist1[Ctsk]* mice followed by compensatory expansion of CTSK[-] lineage sutural cells (Fig. 1f-i, Extended Data Fig. 2).   The presence of a fusion phenotype only in *iDTR[Ctsk]* but not in *Osx[Ctsk]* indicates that it is the absence of CTSK[+] CSCs themselves and not the absence of more mature osterix-dependent osteoblast populations in the CTSK lineage that drive the fusion phenotype.

These results pointed to the existence of a second calvarial stem cell within the pool of CTSK[-] lineage sutural cells. To identify this second CTSK[-] calvarial stem cell, candidate markers of this population were identified by transcriptional analysis and immunostaining (Extended Data Fig. 3a-c). Among these candidates, the transmembrane collagen receptor DDR2 was prioritized based on reports that *Ddr2* is expressed in the sutures and mutant mice display calvarial mineralization defects[7−9]. Our data showed that *Ddr2* was significantly expressed on CTSK[-] lineage sutural cells in *Twist1[Ctsk]* mice (Extended Data Fig. 3d), and DDR2 marked a sutural population not overlapping with CTSK^{+} lineage cells as well as the regions of endochondral ossification (Fig. 2a, Extended Data Fig. 3e). Consistent with the expansion of CTSK^{-} lineage cells observed above, both *Twist1[Ctsk]* and *iDTR[Ctsk]* mice displayed marked expansion of DDR2^{+} sutural cells within the CTSK^{-} population. This included a subpopulation bearing the same surface immunophenotype as CTSK^{+} CSCs, Lin^{-}/Thy-1.2^{-}/6C3^{-}/CD200^{+}/CD105^{-} cells that we hypothesized represent a new population of calvarial stem cells expressing DDR2 (DDR2^{+} CSCs) (Fig. 2b-d, Extended Data Fig. 3f).

Serial transplantation, analysis of differentiation hierarchy, lineage tracing, and label retention studies were used to identify that putative DDR2^{+} CSCs are indeed stem cells. Single clones of DDR2^{+} CSCs were capable of *in vitro* tri-lineage differentiation into osteoblasts, adipocytes, and, separately, chondrocytes

(Extended Data Fig. 3g). *In vivo* transplantation showed that DDR2+ CSCs, but not other DDR2+ populations, were able to both self-renew and generate all of the other DDR2+ populations present in the native suture after the first round of transplantation (Fig. 2e-g, Extended Data Fig. 4). When re-isolated after the first round of transplantation and subjected to the second round of transplantation, DDR2+ CSCs were capable of similar self-renewal and differentiation, demonstrating serial transplantation and self-renewal capacity similar to other skeletal stem cell (SSC) populations identified in long bones[1,10]. Transplantation also clarified that DDR2 is present on the entire lineage of cells derived from DDR2+ CSCs. No evidence of interconversion between DDR2+ CSCs or CTSK+ CSCs was observed (Fig. 2f, Extended Data Fig. 4a).

Another method used to distinguish stem from non-stem skeletal populations is *in vivo* pulse-chase lineage tracing, where targeting stem populations results in durable labeling that disseminates to other downstream populations but targeting non-stem populations results in transient labeling[11]. *Ddr2-CreER;mTmG* mice were used for pulse-chase labeling of DDR2-lineage calvarial cells. *Ddr2-CreER* labeled both suture resident cells and bone-adjacent osteoblasts and showed good concordance with DDR2+ flow cytometry (Fig. 2h, i, Extended Data Fig. 5). Consistent with DDR2+ cells including a stem population, a single early tamoxifen pulse provided durable labeling that was retained in the suture at least 3 months later.

Label retention in the H2B-GFP system has been used across many organ systems as a sensitive method to define slow-cycling stem cells[12–15]. Consistent with the result of transplantation-based stemness assays, H2B-GFP retention was observed in DDR2+ CSCs but not other DDR2+ populations at 6 and 12 months (Fig. 2j-l, Extended Data Fig. 6a, b). In line with the model that the suture contains two separate stem cells, DDR2+ CSCs and CTSK+ CSCs, additional, separate label-retaining cells were observed in the fraction of DDR2- cells bearing markers consistent with CTSK+ CSCs (Lin-/CD200+/CD105-/Thy-1.2-/6C3- cells). As it was not possible to use GFP-based reporters of the CTSK lineage together with the H2B-GFP system, we sought alternative markers of the CTSK+ CSC lineage to confirm the additional presence of label-retaining CTSK+ CSCs, identifying that Galectin-1 immunostaining shows high concordance with *Ctsk-Cre* based lineage reporters (Extended Data Fig. 6c). Using Galectin-1, the label retention in DDR2- CSCs was confirmed to localize to CTSK+ CSCs (Extended Data Fig. 6d). Thus, there are separate pools of label-retaining cells (LRCs) corresponding to both DDR2+ CSCs and CTSK+ CSCs, consistent with the presence of a dual set of stem cells in the calvarium.

Next, we evaluated whether these DDR2+ CSCs are capable of differentiating into bone-forming osteoblasts and whether they mediate endochondral ossification accounting for the inappropriate sutural endochondral ossification seen in *Twist1Ctsk* mice. Indeed, DDR2+ CSCs isolated by FACS and transplanted to the kidney capsule of hosts engrafted and formed robust bone organoids, forming significantly more bone on a per cell basis than CTSK+ CSCs (Fig. 3a-c). This bone was derived from graft DDR2+ CSCs, as graft bone tissue was densely populated with osteocytes bearing the tdTomato marker

of graft DDR2^{+} CSCs (Fig. 3d). Additionally, no interconversion between DDR2^{+} CSCs and CTSK[+] CSCs could be observed as there was no induction of *Ctsk-Cre* driven mGFP expression in the DDR2^{+} CSCs over time, consistent with the result of the serial transplantation study.

Whereas CTSK[+] CSCs mediated the expected intramembranous ossification after transplantation[1], DDR2^{+} CSCs underwent endochondral ossification consistent with being mediators of the inappropriate sutural endochondral ossification seen in *Twist1[Ctsk]* mice (Fig. 3e, Extended Data Fig. 7a). However, while endochondral ossification is intrinsically coupled with the recruitment of hematopoietic marrow elements[1,16], DDR2^{+} CSCs mediate a distinct form of endochondral ossification without recruitment of hematopoietic cells (Fig. 3f, Extended Data Fig. 7b). While the etiology of this difference is likely multifactorial, DDR2^{+} CSC-derived organoids did not produce cells expressing the hematopoietic niche factor CXCL12 (Extended Data Fig. 7c) in contrast with organoids from long bone SSCs[17].   Taken together, this indicates that a third fundamental form of bone formation, endochondral ossification without hematopoiesis, exists alongside traditional intramembranous and endochondral ossification, and DDR2^{+} CSCs are specialized for this third form of bone formation.

Transcriptional profiling of DDR2^{+} CSCs vs CTSK[+] CSCs established that these cells each display broadly distinct transcriptional profiles, reinforcing that DDR2^{+} CSCs vs CTSK[+] CSCs are distinct cell types (Fig. 3g). GLI1 was expressed in both CTSK[+] CSCs and DDR2^{+} CSCs (Extended Data Fig. 8a, b) suggesting that this schema resolves the pool of Gli1-lineage calvarial progenitors into multiple discrete stem cell types[18]. Consistent with the chondrogenic capacity of DDR2^{+} CSCs, these cells expressed higher levels of classically chondrocyte-associated transcripts such as *Sox9*, *Col2a1*, and *Acan*, though these transcripts were also present at lower levels in CTSK[+] CSCs. Both CTSK[+] CSCs and DDR2^{+} CSCs share the expression of several general stem cell, SSC-associated transcripts, including *Myc*, *Runx2*, *Klf4*, and *Nes*[1,19–21]. They showed enrichment of many genes involved in embryonic suturogenesis including *Msx1/2*[22], *Acta2*, *Lgr5*, and *Lrig1*[23]*,* and similarly co-expressed *Axin2*[24], *Prrx1*[25], and *Gli1*[26]*,* genes previously used to study calvarial stem cell populations (Fig. 3h, Extended Data Fig. 8c). Interestingly, many of these shared genes were also present in both periosteal and endosteal stem cells[1], and growth plate resident SSCs[27] in long bones, indicating convergence on a set of SSC-defining genes shared among multiple SSC types at different skeletal sites. Lastly, a number of genes associated with human craniosynostosis are expressed at higher levels in DDR2^{+} CSCs, including *Efnb1*, *Zic1*, *Ihh*, *Msx2*, *Fgfr2*, and *Fgfr3*[28–31] (Extended Data Fig. 8d).

In addition to a role in craniosynostosis, DDR2^{+} CSCs have an important contribution to calvarial mineralization distinct from that of CTSK[+] CSCs. Inducible postnatal deletion of DDR2^{+} CSCs in *Ddr2-CreER;DTA* mice resulted in enlargement of the anterior fontanelle due to hypomineralization of the frontal bones and parietal bones, and severe hypomineralization of the interparietal bones (Fig. 4a). Similarly, deletion of *Osx* specifically in DDR2^{+} CSCs (*Osx^{fl/fl};Ddr2-CreER*) resulted in calvarial hypomineralization similar to that seen in *Ddr2-CreER;DTA* mice (Fig. 4b). Interestingly, DDR2 itself

appears to be functional on DDR2+ CSCs, as mice with the spontaneously occurring smallie mutation causing a loss of function in DDR2 (*Ddr2slie* mice) display calvarial hypomineralization[8] especially evident in the parietal and frontal bones (Extended Data Fig. 9a). *Ddr2slie* mice also displayed an absence or reduction in the cartilage structures in the lateral portions of the interparietal and occipital bones, implicating DDR2+ CSCs in the formation of the cartilaginous elements of the calvarium (Extended Data Fig. 9b, c).

Using an orthotopic transplantation model[32,33] where a native lambdoid suture is surgically ablated and then replaced with a cell pellet of defined composition (Fig. 4c, Extended Data Fig. 10a), DDR2+ CSCs were sufficient to promote fusion in a manner that is restrained by CTSK+ CSCs (Fig. 4d). DDR2+ CSCs, but not CTSK+ CSCs, were sufficient to mediate fusion not only at the implantation site (the LAM suture), but also in an extended region of the SAG, OIP, and SQ sutures adjacent to the implantation site, despite both populations being capable of robust engraftment (Fig. 4e, Extended Data Fig. 10b-d). This fusion in adjacent regions reflected migration of graft DDR2+ CSCs to these sites, in addition to the retention of the graft cells at the primary implantation site (Extended Data Fig. 10e, f). Consistent with finding that depletion of CTSK+ CSCs was sufficient to induce suture fusion, co-implantation of CTSK+ CSCs with DDR2+ CSCs prevented the fusion-promoting activity of DDR2+ CSCs, while not impacting their ability to engraft. This fusion-suppressing ability of CTSK+ CSCs reflected continuous, direct regulation and not induced death or differentiation of DDR2+ CSCs as co-implantation of CTSK+ CSCs and DDR2+ CSCs followed by post-transplantation ablation of the implanted CTSK+ CSCs using a diphtheria toxin (DT) system was able to restore the fusion activity of DDR2+ CSCs (Fig. 4f-h, Extended Data Fig. 11).

Lastly, human counterparts of DDR2+ CSCs are present in the sutures of patients with craniosynostosis, establishing the clinical relevance of this SSC type. Consistent with prior literature[34,35] and observations in *Twist1Ctsk* mice, calvarial specimens from patients with sporadic craniosynostosis displayed inappropriate endochondral ossification with cartilage undergoing active remodeling into the bone and contained abundant DDR2+ cells (Fig. 5a, b). Human sutural tissue also included both DDR2+ and DDR2- cells bearing a surface immunophenotype nearly identical to murine DDR2+ CSCs and CTSK+ CSCs (Lin-/Thy-1-/CD200+/CD105- cells that are DDR2+ or DDR2-, hereafter hDDR2+ CSCs and hDDR2- CSCs, Fig. 5c). Given the inability to utilize CTSK-based lineage reporters in humans, hDDR2- CSCs were here utilized as a proxy for murine CTSK+ CSCs. Interestingly, this hCSC definition also largely overlapped with another set of markers used to define stem cells in human fetal long bones (PDPN+/CD146-/CD164+/CD73+)[36] (Extended Data Fig. 12a). Thus, hDDR2+ and hDDR2- CSCs show a convergent immunophenotype that fulfills criteria from multiple schema for identifying SSCs. Both hDDR2- and hDDR2+ CSCs were capable of forming bone in xenograft systems, with the hDDR2+ CSCs isolated from craniosynostosis patients showing a much greater per-cell bone tissue formation capacity (Fig. 5d). Additionally, consistent with observations that murine DDR2+ CSCs are specialized for endochondral ossification without recruitment of hematopoietic elements, hDDR2+ CSCs mediated

endochondral bone formation (Fig. 5e). Moreover, both DDR2$^+$ CSCs and DDR2$^-$ CSCs displayed evidence of stemness, as both were able to generate the populations present in the initial donor suture tissue in addition to self-renewing or maintaining the input cell type (Fig. 5f, Extended Data Fig. 12b, c).

In summary, we here find that the calvarial sutures contain two distinct stem cell types. One is a CTSK$^+$ CSC that is specialized for intramembranous bone formation. A second identified here is a DDR2$^+$ CSC that characteristically mediates endochondral ossification without marrow formation. Interactions between these two cells are critical for the pathogenesis of craniosynostosis and suture patency, as dropout of CTSK$^+$ CSCs triggers a maladaptive expansion and activation of DDR2$^+$ CSCs, which in turn results in inappropriate endochondral ossification in the sutures and, ultimately, fusion. Both of these cell types are also present in human calvarial sutures (Fig. 5g). Given their role in craniosynostosis, agents that inhibit DDR2$^+$ CSCs or otherwise block their compensatory expansion offer an attractive strategy for adjunct medical therapy of craniosynostosis. Moreover, this provides an example of how multiple skeletal stem cell lineages can co-exist and interact at a single site, with disruptions in these stem cell to stem cell interactions serving as a new mechanism for skeletal disease.

Declarations

Acknowledgements

Author contributions

S.B. designed, conducted, and analyzed the majority of experiments. M.B.G. and S.D. supervised the project. M.B.G., S.D., and S.B. conceived the project. S.B. and A.R.Y. performed all mouse surgeries. S.B., A.R.Y., and M.C. maintained and genotyped all mice. J.M., T.B., and P.B. supervised or conducted flow cytometry. S.Lalani and T.Z. performed RNA-seq data analysis. M.E.R., T.A.I., C.E.H., and S. Lakhani provided access to human samples and supervised human studies. Z.L. and B.R.S. helped with human sample processing. S.B. and M.B.G. prepared the manuscript. All authors read and approved the manuscript. R.T.F., R.T.C., F.M., C.G., and B.H.G. assisted with mouse cross-generation and participated in data analysis and interpretation. M.C. and B.R.S. performed μCT scans and analysis. J.S. and Z.L.

contributed to methodology development for serial transplantation and label-retention system and data collection.

Competing interest declaration The authors declare no competing interests.

Correspondence and materials requests should be addressed to M.B.G.

References

1. Debnath, S. *et al.* Discovery of a periosteal stem cell mediating intramembranous bone formation. *Nature* **562**, 133–139 (2018).

2. Howard, T. D. *et al.* Mutations in TWIST, a basic helix–loop–helix transcription factor, in Saethre-Chotzen syndrome. *Nat. Genet.* **15**, 36–41 (1997).

3. Ghouzzi, V. El *et al.* Mutations of the TWIST gene in the Saethre-Chotzene syndrome. *Nat. Genet.* **15**, 42–46 (1997).

4. Behr, B., Longaker, M. T. & Quarto, N. Craniosynostosis of coronal suture in Twist1 +/-mice occurs through endochondral ossification recapitulating the physiological closure of posterior frontal suture. *Front. Physiol.* (2011). doi:10.3389/fphys.2011.00037

5. Henry Goodnough, L. *et al.* Twist1 mediates repression of chondrogenesis by β-catenin to promote cranial bone progenitor specification. *Dev.* (2012). doi:10.1242/dev.081679

6. He, F. & Soriano, P. Dysregulated PDGFRα signaling alters coronal suture morphogenesis and leads to craniosynostosis through endochondral ossification. *Dev.* (2017). doi:10.1242/dev.151068

7. Binrayes, A., Ge, C., Mohamed, F. F. & Franceschi, R. T. Role of Discoidin Domain Receptor 2 in Craniofacial Bone Regeneration. *J. Dent. Res.* 002203452110074 (2021). doi:10.1177/00220345211007447

8. Ge, C. *et al.* Discoidin Receptor 2 Controls Bone Formation and Marrow Adipogenesis. *J. Bone Miner. Res.* **31**, 2193–2203 (2016).

9. Mohamed, F., Ge, C., Binrayes, A. & Franceschi, R. T. Discoidin domain receptor 2 functions in skeletal progenitor cells and chondrocytes to control cartilage growth and postnatal bone formation. in *ASBMR 2019 Annual Meeting* (J. Bone Miner. Res. 32, 2019).

10. Chan, C. K. F. *et al.* Identification and specification of the mouse skeletal stem cell. *Cell* **160**, 285–98 (2015).

11. Ono, N., Ono, W., Nagasawa, T. & Kronenberg, H. M. A subset of chondrogenic cells provides early mesenchymal progenitors in growing bones. *Nat. Cell Biol.* **16**, 1157–67 (2014).

12.	Kanda, T., Sullivan, K. F. & Wahl, G. M. Histone-GFP fusion protein enables sensitive analysis of chromosome dynamics in living mammalian cells. *Curr. Biol.* **8**, 377–85 (1998).

13.	Foudi, A. *et al.* Analysis of histone 2B-GFP retention reveals slowly cycling hematopoietic stem cells. *Nat. Biotechnol.* **27**, 84–90 (2009).

14.	Blanpain, C., Lowry, W. E., Geoghegan, A., Polak, L. & Fuchs, E. Self-renewal, multipotency, and the existence of two cell populations within an epithelial stem cell niche. *Cell* **118**, 635–48 (2004).

15.	Wilson, A. *et al.* Hematopoietic stem cells reversibly switch from dormancy to self-renewal during homeostasis and repair. *Cell* **135**, 1118–29 (2008).

16.	Chan, C. K. F. *et al.* Endochondral ossification is required for haematopoietic stem-cell niche formation. *Nature* **457**, 490–4 (2009).

17.	Greenbaum, A. *et al.* CXCL12 in early mesenchymal progenitors is required for haematopoietic stem-cell maintenance. *Nature* **495**, 227–230 (2013).

18.	Zhao, H. *et al.* The suture provides a niche for mesenchymal stem cells of craniofacial bones. *Nat. Cell Biol.* **17**, 386–96 (2015).

19.	Méndez-Ferrer, S. *et al.* Mesenchymal and haematopoietic stem cells form a unique bone marrow niche. *Nature* **466**, 829–34 (2010).

20.	Li, Y. *et al.* Murine embryonic stem cell differentiation is promoted by SOCS-3 and inhibited by the zinc finger transcription factor Klf4. *Blood* **105**, 635–637 (2005).

21.	Cartwright, P. *et al.* LIF/STAT3 controls ES cell self-renewal and pluripotency by a Myc-dependent mechanism. *Development* **132**, 885–896 (2005).

22.	Alappat, S., Zhang, Z. Y. & Chen, Y. P. Msx homeobox gene family and craniofacial development. *Cell Res.* **13**, 429–42 (2003).

23.	Holmes, G. *et al.* Integrated Transcriptome and Network Analysis Reveals Spatiotemporal Dynamics of Calvarial Suturogenesis. *Cell Rep.* **32**, 107871 (2020).

24.	Maruyama, T., Jeong, J., Sheu, T.-J. & Hsu, W. Stem cells of the suture mesenchyme in craniofacial bone development, repair and regeneration. *Nat. Commun.* **7**, 10526 (2016).

25.	Wilk, K. *et al.* Postnatal Calvarial Skeletal Stem Cells Expressing PRX1 Reside Exclusively in the Calvarial Sutures and Are Required for Bone Regeneration. *Stem Cell Reports* **8**, 933–946 (2017).

26.	Zhao, H. *et al.* The suture provides a niche for mesenchymal stem cells of craniofacial bones. *Nat. Cell Biol.* **17**, 386–396 (2015).

27.   Hallett, S. A. *et al.* Chondrocytes in the resting zone of the growth plate are maintained in a Wnt-inhibitory environment. *Elife* **10**, (2021).

28.   Klopocki, E. *et al.* Copy-Number Variations Involving the IHH Locus Are Associated with Syndactyly and Craniosynostosis. *Am. J. Hum. Genet.* **88**, 70–75 (2011).

29.   Twigg, S. R. F. *et al.* Gain-of-Function Mutations in ZIC1 Are Associated with Coronal Craniosynostosis and Learning Disability. *Am. J. Hum. Genet.* **97**, 378–388 (2015).

30.   Twigg, S. R. F. & Wilkie, A. O. M. A Genetic-Pathophysiological Framework for Craniosynostosis. *Am. J. Hum. Genet.* **97**, 359–77 (2015).

31.   Wilkie, A. O. M., Johnson, D. & Wall, S. A. Clinical genetics of craniosynostosis. *Curr. Opin. Pediatr.* **29**, 622–628 (2017).

32.   Yu, M. *et al.* Cranial Suture Regeneration Mitigates Skull and Neurocognitive Defects in Craniosynostosis. *Cell* **184**, 243-256.e18 (2021).

33.   Menon, S. *et al.* Skeletal stem and progenitor cells maintain cranial suture patency and prevent craniosynostosis. *Nat. Commun.* **12**, 4640 (2021).

34.   Goodnough, L. H. *et al.* Twist1 mediates repression of chondrogenesis by β-catenin to promote cranial bone progenitor specification. *Development* **139**, 4428–38 (2012).

35.   He, F. & Soriano, P. Dysregulated PDGFRα signaling alters coronal suture morphogenesis and leads to craniosynostosis through endochondral ossification. *Development* **144**, 4026–4036 (2017).

36.   Chan, C. K. F. *et al.* Identification of the Human Skeletal Stem Cell. *Cell* **175**, 43-56.e21 (2018).

37.   Nakamura, T. *et al.* Estrogen Prevents Bone Loss via Estrogen Receptor α and Induction of Fas Ligand in Osteoclasts. *Cell* **130**, 811–823 (2007).

38.   Chen, Y.-T., Akinwunmi, P. O., Deng, J. M., Tam, O. H. & Behringer, R. R. Generation of aTwist1 conditional null allele in the mouse. *genesis* **45**, 588–592 (2007).

39.   Nakashima, K. *et al.* The Novel Zinc Finger-Containing Transcription Factor Osterix Is Required for Osteoblast Differentiation and Bone Formation. *Cell* **108**, 17–29 (2002).

40.   Peng, Y. *et al.* Increased transport of acetyl-CoA into the endoplasmic reticulum causes a progeria-like phenotype. *Aging Cell* **17**, e12820 (2018).

41.   Cowling, R. T. *et al.* Discoidin domain receptor 2 germline gene deletion leads to altered heart structure and function in the mouse. *Am. J. Physiol. Heart Circ. Physiol.* **307**, H773-81 (2014).

42.   Tumbar, T. *et al.* Defining the epithelial stem cell niche in skin. *Science* **303**, 359–63 (2004).

43.   Sun, J. *et al.* SLITRK5 is a negative regulator of hedgehog signaling in osteoblasts. *Nat. Commun.* **12**, 4611 (2021).

44.   Bok, S. *et al.* MEKK2 mediates aberrant ERK activation in neurofibromatosis type I. *Nat. Commun.* **11**, 5704 (2020).

45.   Love, M. I., Huber, W. & Anders, S. Moderated estimation of fold change and dispersion for RNA-seq data with DESeq2. *Genome Biol.* **15**, 550 (2014).

46.   Zhu, A., Ibrahim, J. G. & Love, M. I. Heavy-tailed prior distributions for sequence count data: removing the noise and preserving large differences. *Bioinformatics* **35**, 2084–2092 (2019).

47.   Huang, D. W., Sherman, B. T. & Lempicki, R. A. Systematic and integrative analysis of large gene lists using DAVID bioinformatics resources. *Nat. Protoc.* **4**, 44–57 (2009).

48.   Huang, D. W., Sherman, B. T. & Lempicki, R. A. Bioinformatics enrichment tools: paths toward the comprehensive functional analysis of large gene lists. *Nucleic Acids Res.* **37**, 1–13 (2009).

Methods

Animals. Cathepsin K-Cre (*Ctsk-Cre*) mice were a gift from S. Kato (University of Tokyo) and T. Nakamura (Tokyo Dental College)[37], Floxed Twist1 (*Twist1*$^{fl/fl}$, Stock 016842-UNC) mice were obtained from the Mutant Mouse Resource & Research Centers (MMRRC)[38], Floxed Osterix (*Osx*$^{fl/fl}$) mice were a gift from B. de Crombrugghe (University of Texas M.S. Anderson Cancer Center)[39], *Ddr2*^{slie} mice on the C57Bl6/J background were a gift from R. T. Franceschi[8]. mTmG (Stock 007676), ROSA26iDTR (Stock 007900), ROSA-DTA (Stock 009669), MIP-GFP (Stock 006864), NOD scid gamma (NSG)-EGFP mice (Stock 021937), pTRE-H2BGFP (Stock 005104) mice were purchased from the Jackson Laboratories. ROSA:LNL:tTA mice (JAX, Stock 011008) were a gift from L. Puglielli (University of Wisconsin-Madison)[40]. *Ddr2-CreER (MerCreMer)* mice were generated by R. T. Cowling and B. H. Greenberg with assistance from the Transgenic Core and Embryonic Stem Cell shared resource at UCSD. Briefly, a MerCreMer cassette was inserted in-frame into exon 2 of DDR2 using homologous recombination following a strategy similar to what was previously described[41] (Extended Data Fig. 13a). The 4.4 kb left homology arm (LHA), amplified by primer' 5'-AACGCGTTGGATCTGGAGTCTGCAGCCCACCGACA'-3' an' 5' GGAGATGCAGGCCATGTTGCCCCAACACCTCCCAT'-3', and the 4.0 kb right homology arm (RHA), amplified by primer' 5'-ACTCCACAGTGCCAAAGATGGTGCCTGAAGCCATG'-3' an' 5'-GCGGCCGGGTTCCCAAGATCTCAGGTAAGCTTTTG'-3', were each individually cloned into a pCR-BluntII-TOPO vector (Life Technologies). A pBKSII-MerCreMer-Mc1-neo vector (provided by Dr. Sylvia Evans, UCSD) was digested by NotI and partially by NcoI (cutting at position 60) to create a NcoI/NotI MerCreMer-neoR cassette that was then ligated into the MluI/NotI sites of the pCR-BluntII-LHA vector using a MluI-HindIII-NcoI adapter. The pCR-BluntII-LHA vector with the MerCreMer-neoR insert was digested with NotI, dephosphorylated, and ligated into the Eag1 site upstream of the RHA in the pCR-

BluntII-RHA vector. A diptheria toxin A (DTA) coding cassette (PspOMI/NotI fragment, provided by Dr. Ju Chen, UCSD) was ligated into the dephosphorylated NotI site distal to the RHA of the pCR-BluntII-LHA-MerCreMer-neoR-RHA vector to provide negative selection. The targeting vector was linearized with NotI and electroporated into 129R1 mouse ES cells. Individual G418-resistant clones were initially screened by PCR and then followed by Southern blot, using KpnI digestion with Probe C and BamHI digestion with Probe D, to identify positive clones (Extended Data Fig. 13b). One targeted clone was microinjected into C57Bl/6 blastocysts that were implanted into pseudopregnant female hosts to generate chimeric pups. Breeding of chimeric animals generated agouti pups that were screened for the targeted mutation. Targeted mice were bred with a FLatrigter mouse (provided by Dr. Ju Chen, UCSD) to remove the neomycin resistance (neoR) cassette prior to backcrossing onto C57Bl/6 for at least 10 generations. Cardiac fibroblasts from a tamoxifen-treated *Ddr2-CreER* mouse were used to validate protein expression of the MerCreMer (Extended Data Fig. 13c), then the mice crossed with mTmG mice. Recipient heterozygous MIP-GFP mice were generated by breeding homozygous MIP-GFP males with wildtype C57Bl6/J females. All mice were maintained on a C57Bl6/J background throughout the study. All animals were maintained in accordance with the NIH Guide for the Care and Use of Laboratory Animals and were handled according to protocols approved by the Weill Cornell Medical College subcommittee on animal care (IACUC).

Diphtheria toxin (DT) and tamoxifen (TAM) administration. *iDTR;Ctsk-Cre;mTmG* pups were given 50 ng of DT (Sigma, cat. D0564) intraperitoneally as indicated in Extended Data Fig. 2a. PBS was used as a vehicle. For lineage tracing analysis, *Ddr2-CreER* activity was induced at postnatal day 2 (P2). TAM (100 mg/kg; Sigma, cat. T5648) was prepared in corn oil and subcutaneously injected into animals for 2 consecutive days as described in Extended Data Fig. 5a. To investigate the physiologic contribution of DDR2$^+$ CSCs, ROSA-DTA and *Osx$^{fl/fl}$* mice were crossed with *Ddr2-CreER;mTmG* mice and TAM was delivered subcutaneously into P7 pups.

Histone H2B-GFP labeling retention system. pTRE-H2BGFP mice were previously described[42]. To label slow-cycling cells under the control of a tetracycline response element, pTRE-H2BGFP mice were crossed with ROSA:LNL:tTA (tet-off) mice. 8-week-old mice were fed with a doxycycline rodent diet (200 mg/kg; Bio-Serv, cat. S3888) for 6 and 12 month chase periods.

Human specimens. This study was carried out under the IRB protocol (no. 1402014802), with all patients providing informed consent through the Center for Neurogenetics at Weill Cornell Medical Center. Human calvarium materials used for scientific analyses were obtained from 24 case specimens that were left over from craniosynostosis surgical repair procedures. Participants had an age range of less than 1 year old and were 80% male.

Isolation of suture cells. For murine samples, microdissected calvarial sutures were subjected to both mechanical and enzymatic digestion. The harvested tissues were minced using razor blades and digested for up to 20 minutes with digestion cocktail buffer containing Collagenase P (1 mg/ml; Roche, cat. 11213857001) and Dispase II (2 mg/ml; Roche, cat. 04942078001) in medium containing 2% serum

at 37 °C with agitation. Medium containing 2% serum was added to the digest and the tubes were centrifuged to pellet cells. The supernatant was carefully removed, and the pellet was resuspended in DNase I (2 units/ml) solution and briefly incubated for 5 min at 37 °C. Media was added to the tube and the digested tissue was re-suspended thoroughly by pipetting and then filtered through a 70-micron nylon mesh. Tubes were centrifuged and the resulting cell pellet was subjected to FACS. For human calvarium specimens, tissues were subjected to mechanical and enzymatic digestion with Collagenase A (1 mg/ml; Roche, cat. 10103586001) and Dispase II (2 mg/ml) in a medium containing 2% serum for 30 min at 37 °C under agitation, and the cells were then isolated following the same procedure as described above.

Fluorescence-activated cell sorting (FACS).   Prepared single-cell suspensions were washed twice with ice-cold FACS buffer (2% serum + 1 mM EDTA in PBS) and incubated with Fc blocking buffer (1:100 dilution; BD bioscience, cat. 553142 for mouse and cat. 564765 for human) for 15 min at 4 °C. Primary antibody dilutions were prepared in Brilliant Stain Buffer (BD bioscience, cat. 563794). Cells were incubated in the dark for 40 min at 4 °C with primary antibody solution, washed 2 times with FACS buffer, and incubated with secondary antibody solution for 20 min, if needed. Cells were then washed several times and re-suspended in FACS buffer with DAPI (BD bioscience, cat. 564907). FACS was performed using a Becton Dickinson Aria II equipped with 5 lasers (BD bioscience). Beads (Invitrogen, cat. 01-3333-42) were used to set initial compensation. Fluorescence minus one (FMO) controls were used for additional compensation and to assess background levels for each stain. Gates were drawn as determined by internal FMO controls to separate positive and negative populations for each cell surface marker. Typically, 2.5 million events were recorded for each FACS analysis, and the data were analyzed using FlowJo (v10.6.1). To better depict the FACS gating strategy, color boxes and arrows have been added to the plot to illustrate parent/daughter gates. Additionally, Extended Data Figures have been provided to show the full details of the gating strategies used (Extended Data Fig. 1a, 3f, 4b, 6a, 6b, 11a).

FACS antibodies.   Antibodies for FACS of murine samples included CD31 (MEC13.3, BD Bioscience), CD45 (clone 30-F11, BD Bioscience), Ter119 (clone TER-119, BD Bioscience), CD249/BP-1 (clone 6C3, eBioscience), Thy-1.2 (clone 53-2.1, BD Bioscience), CD200 (clone OX-90, BD Bioscience), CD105 (clone MJ7/18, BioLegend), DDR2 (clone 102, Novus Biologicals), CD146 (clone ME-9F1, BD Bioscience). Antibodies for FACS of human samples included CD31 (clone WM59, BioLeged), CD45 (clone HI30, BioLeged), CD235a (clone GA-R2, BioLeged), Thy-1 (clone 5E10, BD Bioscience), CD200 (clone MRC OX-104, BD Bioscience), CD105 (clone 43A3, BioLegend), DDR2 (clone 290804, R&D systems; polyclonal, LSBio), CD146 (clone P1H12, BD Bioscience), Podoplanin (clone LpMab-17, BD Bioscience), CD73 (clone AD2, BD Bioscience), CD164 (clone N6B6, BD Bioscience), Alexa Fluor 647 Streptavidin (BioLegend) and Brilliant Violet 650 Streptavidin (BioLeged). Detailed information is stated in the Reporting Summary.

Primary cell culture and clonal differentiation assays.   The clonal multipotency of sorted cell populations was evaluated under normoxic conditions. Mouse primary cells were grown in complete MesenCult medium (Stem Cell Technologies, cat. 05501) with stimulatory supplements (Stem Cell Technologies, cat. 05502, 05500). After initial cell plating, cells were left undisturbed and allowed to grow at 37 °C under

humidified conditions for a week. Half of the medium was replaced every 3 days. Cells were passaged once they were 60-70% confluent using cell dissociation reagent (Gibco, cat. A1110501). Cells sorted from human calvarial tissue were cultured under conditions similar to those described above using a commercial medium preparation (Stem Cell Technologies, cat. 05401) with stimulatory supplements (Stem Cell Technologies, cat. 05402). The differentiation potential of 10 colonies derived from single FACS-isolated cell populations was examined. In brief, single sorted cells were plated at a density of 100 cells in 6-well culture plates and allowed to form individual colonies. Initial dispersion of the plated cells as single cells was confirmed by light microscopy. Each of the selected colonies was extracted using a cloning cylinder. The extracted cells were regrown for 3 days in 12-well plates and then allowed to differentiate under both osteogenic and adipogenic conditions as described below. For osteogenic differentiation and Alizarin Red S staining, sorted cells were expanded and then allowed to differentiate using an osteogenic differentiation medium (Gibco, cat. A1007201) for 21 days. The medium was changed every other day. At the end of this period, cells were washed with cold PBS and fixed with 4% PFA for 30 min on ice. Cells were washed with distilled water and stained with Alizarin Red S for 2 min. Cells were then washed thoroughly with water and air-dried before microscopic visualization. Adipogenic differentiation studies were conducted with sorted cells using methods similar to those described above. In brief, cells were allowed to differentiate in adipogenic differentiation medium (Gibco, cat. A1007001). Fresh medium was added every other day for a total of 14–20 days. The medium was removed, and cells were washed with PBS and fixed with 4% PFA for 30 min at room temperature. Cells were rinsed again with PBS and stained for 30 min with Oil Red O working solution (3:2 dilution with water). After washing 5 times with PBS, cells were then observed under a light microscope. For chondrogenic differentiation and Alcian Blue staining, cells were grown as pellet culture. 1×10^4 cells in chondrogenic differentiation medium (Gibco, cat. A1007101) were centrifuged at 1500 rpm for 5 min in 15 ml conical tubes. Cultures were re-fed every 3 days and allowed to differentiate for a minimum of 14 days. At the endpoint of this study, the medium was removed, and pellets were harvested and washed carefully with PBS and fixed with 4% PFA for 30 min, then embedded in OCT compound. After cryo-sectioning, slides were stained for 30 min with 1% Alcian Blue solution, washed three times with 0.1 N HCl, and then with PBS.

μCT scans and analysis.   μCT analysis was conducted on a Scanco Medical μCT 35 system at the Citigroup Biomedical Imaging Core as previously described[43]. Briefly, a Scanco Medical μCT 35 system with an isotropic voxel size of 7 μm and 20 μm were used to image the distal femur/tibia and skull, respectively. Scans were conducted in PBS and used an X-ray tube potential of 55 kVp, an X-ray intensity of 0.145 mA, and an integration time of 600 ms. μCT analysis was performed by an investigator blinded to the genotypes of the animals.

Renal capsule transplant for bone organoids.   Renal capsule transplantation was performed in 8-10 week old MIP-GFP mice as previously described[1]. To avoid potential immunogenicity of GFP itself, all transplantation studies were conducted in MIP-GFP hosts that have baseline immunologic tolerance to GFP variants. Briefly, mice were anesthetized and shaved on the left flank and abdomen before sterilization of the surgical site. The kidney was externalized through a 1 cm incision and a 2 mm pocket

was made in the renal capsule. A 5 atrigelgel plug (Corning, cat.356231) containing the cells of interest was implanted underneath the capsule and the hole was sealed using a cauterizer before replacing the kidney back into the body cavity. Approximately more than 20 donor mice were sacrificed to harvest the desired number of CSCs for every organoid-based transplantation experiment. Animals were euthanized by CO_2 after the indicated experimental duration. After sacrifice, kidneys were fixed with 4% PFA for 6 hrs and bone formation was detected by μCT and fluorescent stereomicroscopes. Samples were subjected to infiltration, embedding, and sectioning as described below.

Intramuscular transplant for differentiation hierarchy. Intramuscular transplantation was performed in 6 to 8-week-old MIP-GFP mice. A 1 mm longitudinal incision was made on the right hindlimb and the right anterolateral femur was exposed. The vastus lateralis muscle was dissected and a 2-3 mm muscle pouch was surgically created. A surgifoam absorbable gelatin sponge (Ethicon, cat. 1972) containing sorted cell populations of interest was placed into the muscle pouch. The overlying fascia was closed by using 4-0 polyglactin 910 absorbable sutures (Ethicon, cat. J386), and wound clips were used to close the skin incision. For serial transplantation studies, animals were euthanized by CO_2 narcosis 7-10 days post-surgery, and the muscle was dissociated for FACS analysis.

Suture ablation model. 4-week-old MIP-GFP mice were anesthetized and had the skin overlying the skull shaved before sterilization of the surgical site. A scalpel was used to carefully remove the periosteum of the skull prior to removing the lambdoid sutures and surrounding bones on the right side of the skull using a micro hand drill with 0.2 mm drill bits (Stoelting, cat. 58610). Cell populations of interest (2×10^4 cells) were isolated by FACS from calvarial sutures of *Ctks-Cre;mTmG* or *iDTR;Ctsk-Cre;mTmG* mice and were mixed with 2 μl of a gel mixture (GelMA:Matrigel:Collagen I, 6:3:1) (Cellink, cat. *IK3051020303*, Corning, cat. 356231, Gibco, cat. A1048301, respectively) prior to implantation at the defect site. The gel mixture, with or without cells, was cross-linked by exposure to UV light for few seconds after transplantation and the skin incision was closed using an absorbable suture. Animals were euthanized by CO_2 and the specimens were collected after 8 and 16 weeks.

Sample preparation for cryo-sectioning and imaging. Freshly extracted mouse samples were fixed with 4% PFA for 4-6 hours at 4 °C. Samples were washed with PBS and decalcified with daily changes of 0.5 M EDTA for 1-5 days depending on the age of the samples. Samples were incubated with infiltration medium (20% sucrose + 2% polyvinylpyrrolidone in PBS) with rocking until they sank to the bottom of the tube. Embedding was performed with a customized embedding medium (OCT + 15% sucrose in PBS) and samples were preserved at −80 °C. Sections, 10-20 μm in thickness, were cut using a Leica cryostat.

Immunohistochemistry. Immunohistochemical analysis was conducted on Zeiss instruments and systems at the Optical Microscopy Core using the previously described[44]. In brief, frozen samples were thawed at room temperature and rehydrated with PBS, permeabilized with 0.3% Triton X-100 in PBS for 10 min and blocked for 30 min with 5% donkey serum in PBS. Dilutions of primary antibodies (1:50-1:100) were freshly prepared in 0.3% Triton X-100 in PBS. Samples were incubated overnight with primary antibodies at 4 °C and, then washed three times with PBS. Secondary antibodies (1:1000 dilution) were

added to samples for 1 hour, followed by washing three times with PBS. Samples were finally mounted with ProLong Gold antifade reagent with DAPI (Invitrogen, cat. P36931). Imaging was performed with a Zeiss LSM 880 laser scanning confocal microscope. All data were processed using Zeiss ZEN 2.3 SP1 software.

Bulk RNA-sequencing. Total mRNA was freshly extracted from FACS-isolated CSC populations from P7 *Ctsk-Cre* mice (n=5) using RNeasy Plus Micro Kit (Qiagen, cat. 74034). Total RNA integrity was checked using a 2100 Bioanalyzer (Agilent Technologies). cDNA synthesis and amplification were performed by SMART-Seq v4 ultra-low input RNA kit (Takara Bio, USA) starting with 1 ng of total RNA from each sample. 150 pg of qualified full-length double strand cDNA was used and processed for Illumina library construction with the Nextera XT DNA Library Preparation Kits (Illumina). Then the normalized cDNA libraries were pooled and sequenced on an Illumina NovaSeq6000 sequencer with pair-end 50 cycles. Bulk RNA-sequencing was performed on a total of 10 FACS-isolated CSC populations (5 CTSK[+] and 5 DDR2^{+}) from mice, and a counts matrix was obtained. DESeqDataSet was generated using this unnormalized counts matrix. Differential expression analysis was performed using the 'DESeq' function and results tables were generated using the 'results' function to compare the DDR2^{+} vs. CTSK[+] groups[45]. Log fold change shrinkage was performed using the 'lfcShrink' function with the 'apeglm' method[46] for visualization and ranking of genes. Results were exported as .csv files (one with all the genes, and one with the subset of genes with adjusted P value < 0.05). 2-D PCA plots of the samples were generated by the first two principal components using the 'plotPCA' function. Normalized read counts were used for generating heatmap plots. The data was visualized by heatmap with hierarchical clustering in R v3.6.2 with the pheatmap package v1.0.12. GO analysis was performed using DAVID Bioinformatics Resource tools v6.8[47,48].

Statistical analyses. All data are shown as mean ± s.d. as indicated. For comparisons between two groups, unpaired, two-tailed Student's *t* tests were used. GraphPad PRISM v7.04 was used for statistical analysis. $P < 0.05$ was considered statistically significant. *$P < 0.05$, **$P < 0.01$, ***$P < 0.001$, and ****$P < 0.0001$.

Extended data figure/table legends

Extended Data Fig. 1 | Analysis of CTSK[+] CSC and CTSK[-] CSC populations in mouse calvarial sutures. a, µCT images of the skull of WT and *Twist1[Ctsk]* mice (P0 WT, n=6 *Twist1[Ctsk]*, n=8; P7 WT, n=8 *Twist1[Ctsk]*, n=5; P14 WT, n=6 *Twist1[Ctsk]*, n=6; P21 WT, n=6 *Twist1[Ctsk]*, n=5; P56 WT, n=9 *Twist1[Ctsk]* n=6). **b**, Representative fluorescent images of the major sutures including the posterior-frontal (PF), coronal (COR), sagittal (SAG), and lambdoid (LAM) sutures in WT and *Twist1[Ctsk]* mice at P21. Green, CTSK^{+} mGFP cells; Red, CTSK^{-} tdTomato cells. Scale bars, 100 µm. **c**, Representative FACS plots and quantification of total cell number of CTSK-lineage cells (CD31^{-}/CD45^{-}/Ter119^{-}/CTSK^{+}) from the major sutures of WT (n=4) and *Twist1[Ctsk]* (n=4) mice at P14. OIP, occipitointerparietal suture. **d**, Gating strategy for FACS analysis of CTSK[+] CSC and CTSK[-] CSC populations in the calvarial suture of *Ctsk-Cre;mTmG*

mice. **e**, No evidence of cartilage clusters in the suture at P25. Representative fluorescent images of the LAM sutures in WT and *Twist1^Ctsk* mice. Green, CTSK$^+$ mGFP cells; Red, CTSK$^-$ tdTomato cells. Scale bars, 100 μm. Lin indicates CD31, CD45, and Ter119 for all FACS analyses. Mean ± s.d., unpaired, two-tailed Student's t test. Images and FACS plots are representative of at least 4 independent experiments.

Extended Data Fig. 2 | In vivo depletion of CTSK$^+$ cells using an inducible DTR (iDTR) system. a, Schematic representation of the experimental design and gross appearances of *ROSA26iDTR* and *iDTR^Ctsk* mice before and after DT administration. The arrow indicates an abnormal dome-shaped skull. **b**, μCT scan images of the skull of *ROSA26iDTR* and *iDTR^Ctsk* mice at P21 after DT administration. Red arrows indicate suture defects with abnormal fusion and hypomineralization. Scale bars, 1.0 mm (*ROSA26iDTR*, n=5; *iDTR^Ctsk*, n=5). **c**, Gross image of the femurs in *ROSA26iDTR* and *iDTR^Ctsk* mice after DT administration. **d-f**, Representative μCT images of the cortical (**d**), trabecular bones (**e**), and tibias (**f**) in *ROSA26iDTR* and *iDTR^Ctsk* mice after DT administration. Arrows show cortical defects including uneven periosteal surfaces and a double cortex.

Extended Data Fig. 3 | Characterization of DDR2$^+$ CSCs. a, **b**, Candidate cell surface markers from gene expression analysis of FACS-purified CTSK$^+$ CSC and CTSK$^-$ CSC populations. **c**, Immunostaining for NGFR (CD271) and NCAM1 (CD56) in the calvarial suture of *Ctsk-Cre;mTmG* mice at P7. Green, CTSK$^+$ mGFP cells; Red, CTSK$^-$ tdTomato cells; Magenta, NGFR (right) or NCAM1 (left). Scale bars, 100 μm. Experiments were repeated 3 independent times. **d**, *Ddr2* mRNA expression in CTSK$^-$ CSCs of WT (n=6) and *Twist1^Ctsk* (n=6) analyzed by qRT-PCR. **e**, Immunostaining for DDR2 in the suture mesenchyme of WT and *Twist1^Ctsk* mice at P14. Green, CTSK$^+$ mGFP cells; Red, CTSK$^-$ tdTomato cells; Cyan, DDR2-expressing cells; Blue, DAPI. Right, enlarged view of the yellow dotted box. Scale bars, 100 μm, 50 μm. **f**, Gating strategy for CTSK-negative DDR2$^+$ CSCs in the calvarial sutures of P7 *Ctsk-Cre;mTmG* mice. **g**, Images of Alcian Blue (i), Alizarin Red S (ii), and Oil Red O (iii) staining for clonal multipotency. All cells were derived from the expansion of a single FACS-isolated CTSK$^+$ CSC or DDR2$^+$ CSC. Images are representative of 5 independent experiments.

Extended Data Fig. 4 | Determination of the stemness and differentiation hierarchy of DDR2$^+$ CSCs. a, FACS plots of tdTomato-DDR2$^+$ CSC and mGFP-CTSK$^+$ CSC populations after the first round of transplantation. Sponges without cells were used as a negative control. **b**, Experimental strategy for *in vivo* differentiation hierarchy study and gating strategy showing serially transplanted cell populations including DDR2$^+$ CSCs (i), DDR2$^+$/Thy-1.2$^-$/6C3$^-$/CD200^v/CD105$^+$ (ii), DDR2$^+$/Thy-1.2$^-$/6C3$^-$/CD200$^-$/CD105$^-$ (iii), DDR2$^+$/Thy-1.2$^+$/6C3$^-$ (iv) of the calvarial suture of primary donor. **c**, FACS analysis of serially transplanted cell populations derived from ii), iii), and iv) populations after the first/second round transplantation. Left plots show cell differentiation of the indicated populations in primary recipients after the first round of transplantation and right plots show these populations in secondary recipients after the second round transplantation. Black and red arrows indicate

parent/daughter gates and transplanted populations, respectively. Experiments were repeated 5 independent times.

Extended Data Fig. 5 | Characterization of *Ddr2-CreER* mice. a, Experimental design for lineage tracing of tamoxifen (TAM)-induced *Ddr2-CreER* mice pulsed at P2. **b**, Short-term chase (10 days) of calvarial suture DDR2$^+$ cells in *Ddr2-CreER;mTmG* mice. Green, DDR2$^+$ mGFP cells; Red, DDR2$^-$ tdTomato cells; Blue, DAPI. Right, enlarged view of the yellow dotted boxes. Scale bars, 100 μm and 20 μm. **c, d**, Fluorescent imaging of osteoblasts derived from DDR2$^+$ cells in *Ddr2-CreER;mTmG* mice as determined by cellular location and morphology (**c**) and osteocalcin (OCN) staining (**d**). Images in **b-d** represent at least 3 independent experiments. **e**, FACS analysis of time-course genetic lineage tracing for DDR2-lineage cells in the calvarial sutures of *Ddr2-CreER;mTmG* mice. Red boxes indicate DDR2$^+$ CSCs (Lin$^-$/DDR2-mGFP$^+$/Thy1.2$^-$/6C3$^-$/CD200$^+$/CD105$^-$).

Extended Data Fig. 6 | Tet-off driven H2B-GFP system to define the LRCs in the calvarial suture. a, b, Gating strategy for H2B-GFP$^+$ LRCs within DDR2$^+$ CSC and DDR2$^-$ CSC populations . Offset histogram overlays displaying GFP fluorescence from Lin$^-$/Thy-1.2$^-$/6C3$^-$/DDR2$^+$ and DDR2$^-$ populations after 6 (**a**) or 12 month (**b**) chase periods. Black arrows indicate parent/daughter gates. **c**, Representative images of immunostaining for Galectin-1 overlapping with CTSK-mGFP cells in mouse calvarium. Green, CTSK$^+$ mGFP cells; Magenta, Galectin-1; Blue, DAPI. Scale bars, 20 μm. **d**, Representative immunostaining images for Galectin-1 in the calvarial sutures of H2B-GFP mice after 12 months of doxycycline exposure. Co-localization is shown by arrows. Green, H2B-GFP; Red, Galectin-1; Blue, DAPI. Scale bars, 10 μm. Images are representative of 3 independent experiments.

Extended Data Fig. 7 | Functional characterization of DDR2$^+$ CSCs. a, Representative immunostaining images of Collagen type II (COLII) in grafts derived from sorted DDR2$^+$ CSCs. Gray, Primary graft; Magenta, COLII; Blue, DAPI. Scale bars, 100 and 10 μm, respectively. **b**, Validation of antibodies for detecting hematopoietic cells in mouse calvarial marrow. Representative immunostaining images for CD45 (green) and CD34 (magenta) at P21 in mouse calvarium. Scale bars, 20 μm. **c**, Immunostaining for CXCL12 in kidney grafts derived from sorted femoral SSC and sutural DDR2$^+$ CSC populations. Green, CXCL12; Red, Primary graft; Blue, DAPI. Scale bars, 100 and 50 μm. Co-localization is shown by white arrows. Images in **a-c** are representative of 3 independent times.

Extended Data Fig. 8 | Transcriptional analysis of CTSK$^+$ CSCs and DDR2$^+$ CSCs isolated from mouse calvarial sutures. a, Immunostaining for GLI1 in the calvarial sutures of *Ctsk-Cre;mTmG* (left) and *Ddr2-CreER;mTmG* (right) mice at P14. Green, CTSK$^+$ mGFP (right); DDR2$^+$ mGFP (left); Magenta, GLI1; Blue, DAPI. Scale bars, 20 μm. Images represent the results of 3 independent experiments. **b**, Normalized *Gli1* read counts determined by RNA-Seq analysis from FACS-isolated CTSK$^+$ CSCs and DDR2$^+$ CSCs in the calvarial suture at P7. **c**, Hierarchical clustering of expression heatmaps showing differentially expressed genes associated with bone development, including endochondral ossification (GO:0001958), positive or negative regulation of cartilage development (GO:0061036; GO:0061037, respectively),

regulation of chondrocyte differentiation (GO:0032330) by Gene Ontology Biological Process analysis from RNA-Sequencing in CTSK[+] CSCs and DDR2^{+} CSCs at P7. **d**, Heatmap generated from murine bulk RNA-Seq analysis of sorted CTSK[+] CSCs and DDR2^{+} CSCs showing differentially expressed genes associated with human craniosynostosis.

Extended Data Fig. 9 | Analysis of *Ddr2^slie* mice. a, μCT scan images of the skull of WT and *Ddr2^slie* mice at P7 and P14. Scale bars, 1.0 mm (P7 WT, n=7 *Ddr2^slie*, n=8; P14 WT, n=5 *Ddr2^slie*, n=6). **b**, Representative images of Alican Blue staining of the calvarial sutures in WT and *Ddr2^slie* mice at P7. Nuclear Fast Red was used as a counterstain. Scale bars, 200 μm. **c**, Whole-mount P3 skull preparations with Alcian Blue staining of WT (n=8) and *Ddr2^slie* (n=9) mice.

Extended Data Fig. 10 | Orthotopic transplantation of calvarial stem cells. a, Surgical field and μCT scan image after ablation of the right lambdoid (LAM) suture in 4-week-old MIP-GFP mice. **b, c**, μCT scans and stereomicroscopic fluorescent images of mouse skulls at 8 and 16 weeks post-transplantation. mGFP-expressing CTSK[+] CSC and tdTomato-expressing DDR2^{+} CSC populations isolated from the calvarial sutures of P7-10 *Ctsk-Cre;mTmG* mice. Each indicated population was implanted into the suture ablation area after carrier encapsulation. The control group was subjected to only the gel mixture carrier without cells. Red arrows indicate the fusing and fused sutures. **d, e**, Fluorescent imaging of transplanted cells derived from FACS-isolated CTSK[+] CSC and DDR2^{+} CSC populations at the primary defect areas, LAM (d) and OIP (e) sutures at 8 weeks post-transplantation. Each red line in μCT images indicates the sectioning area and direction. Green, CTSK[+] mGFP; Red, DDR2^{+} tdTomato; Blue, DAPI. An asterisk denotes the fused suture. Scale bars, 100 μm. **e**, Images of transplanted cells derived from DDR2^{+} CSCs on the SQ sutures at 8 weeks post-transplantation. Scale bars in all μCT images denote 1.0 mm.

Extended Data Fig. 11 | Orthotopic transplantation of calvarial stem cells using lineage ablation system. a, 3D reconstruction of μCT scans of the skull 16 weeks after orthotopic transplantation with subsequent DT administration. (Control, n=6; CTSK[+], n=6; DDR2^{+}, n=5; CTSK[+] and DDR2^{+}, n=5; iDTR;CTSK[+] and DDR2^{+}, n=4). Red arrows indicate the fusing and fused sutures. Scale bars, 1.0 mm. **b**, Fluorescent images of the sutures in mice receiving DDR2^{+} CSC or co-transplanted iDTR;CTSK[+] and DDR2^{+} CSC grafts 16 weeks after orthotopic transplantation with subsequent DT administration. tdTomato and GFP visualization showing engrafted cells at sites of newly formed cranial bone. Each red line in μCT images indicates the sectioning area and direction. Scale bars, 100 μm. Green, CTSK[+] mGFP; Red, DDR2^{+} tdTomato; Blue, DAPI.

Extended Data Fig. 12 | Characterization of human DDR2^{+} CSCs. a, FACS plots for human calvarium tissues. Lin indicates CD31, CD45, and CD235a in human tissue. Red boxes indicate transplanted cell populations including hDDR2^{-} CSCs and hDDR2^{+} CSCs. Orange boxes indicate markers defining human SSC populations (PDPN^{+}/CD146^{-}/CD164^{+}/CD73^{+}), reported in human fetal long bones[36]. **b**, Gross image of NSG-EGFP recipients and a schematic representation of the intramuscular transplantation model for human sutural cells. **c**, FACS plots showing cell differentiation of the indicated input populations

including hDDR2$^+$ CSCs (i), hDDR2$^-$ CSCs (ii), and matrigel only (iii) in primary recipients after transplantation. Matrigel without cells was used as a control. Black arrows demonstrate parent/daughter gates. Experiments underwent 3 independent repeats.

Extended Data Fig. 13 | Generation of *Ddr2-CreER* mice. **a**, Diagram of targeting the MerCreMer cassette in-frame into exon 2 of the murine *Ddr2* gene. Top, targeting location into exon 2 of *Ddr2*; middle, targeting vector; bottom, targeted knock-in allele. Exons are numbered solid black boxes, polyA sites are dark gray boxes, frt sites flanking the neomycin (neo) selection cassette are black arrow heads, the left and right homology arms, LHA and RHA respectively, are light gray boxes. Restriction sites are the following: KpnI (K), BamHI (B), MluI (M), NcoI (n), NotI (N), and NotI destroyed site (N*). MerCreMer, Cre-ER cassette; tk, thymidine kinase promoter; DTA, diptheria toxin A cassette. **b**, Southern blot screening of ES cell clones. Genomic DNA was isolated from a subset of cells and digested with either KpnI, screened with Probe C to produce a 5.5 kb band for positive clones, or BamHI, screened with Probe D to produce a 5.0 kb band for positive clones. WT band size was 10.5 kb. Hybridization regions for Probe C and Probe D are shown in part a. **c**, MerCreMer protein expression in cardiac fibroblasts from a tamoxifen treated *Ddr2-CreER* mouse. WT, wildtype mouse; KI, knock-in mouse.
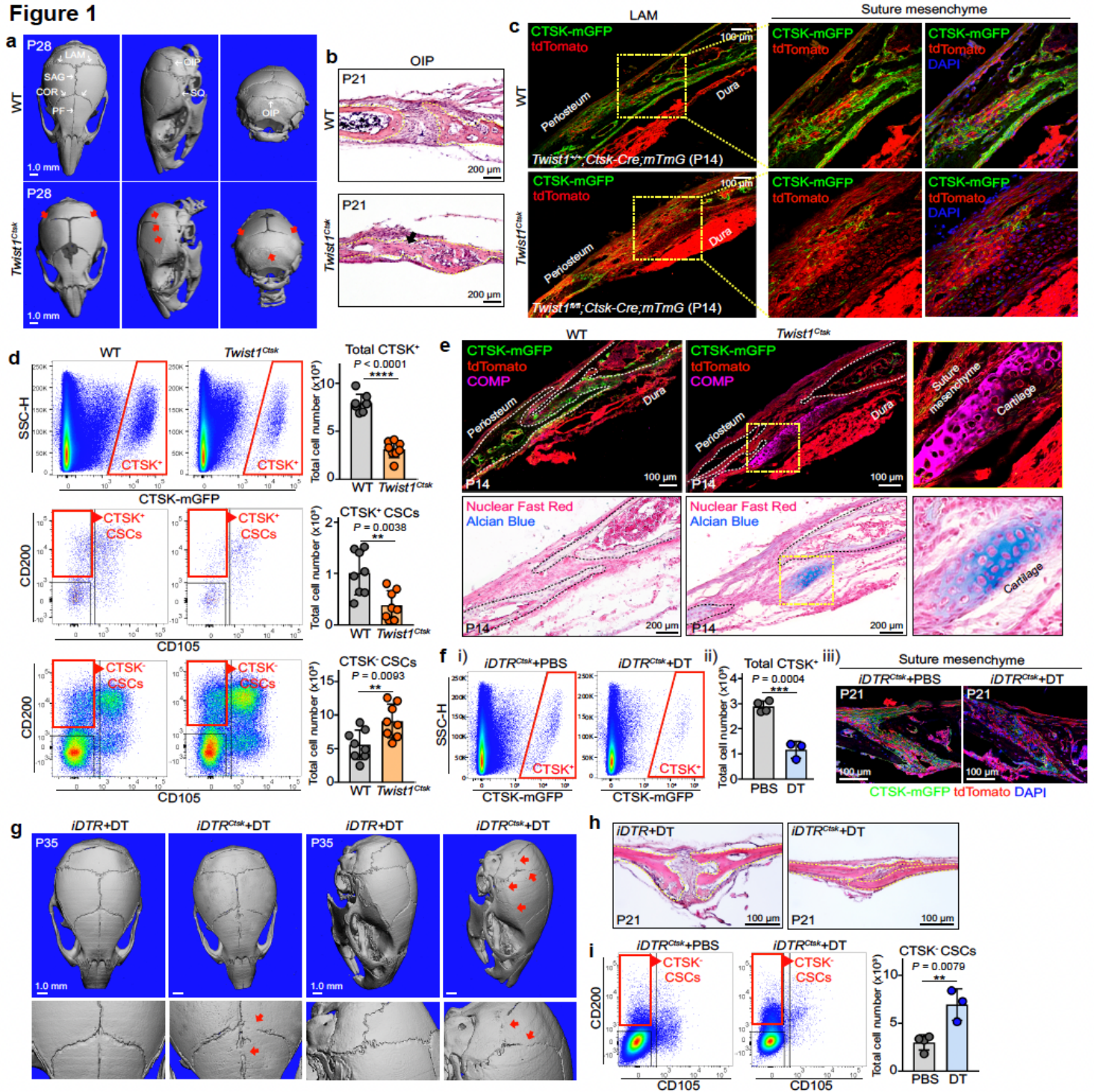
Figures

Figure 1

Defects in CTSK+ CSCs cause craniosynostosis and the expansion of an alternative sutural population. a, μCT images of the skull of WT (Twist1+/+;Ctsk-Cre;mTmG) and Twist1Ctsk (Twist1fl/fl;Ctsk-Cre;mTmG) mice at P28 (WT, n=6; Twist1Ctsk, n=6). Red arrows indicate the fusing and fused sutures. Posterior-frontal (PF); coronal (COR); sagittal (SAG); lambdoid (LAM); squamosal (SQ); occipitointerparietal (OIP) sutures. B, Representative images of H&E staining of the OIP suture in WT and Twist1Ctsk mice at P21. The black arrow indicates the fused suture. Scale bars, 200 μm. c, Representative fluorescent images of

the LAM suture in WT and Twist1Ctsk mice at P14. Green, CTSK+ mGFP cells; Red, CTSK- tdTomato cells; Blue, DAPI. Right, enlarged view of the yellow dotted box in each panel. Scale bars, 100 μm. d, FACS analysis of the distribution of total live CTSK+ mGFP cells (top row), CTSK+ CSCs (Lin-/Thy-1.2-/6C3-/mGFP+/CD200+/CD105-) (middle row), and CTSK-negative CSCs (Lin-/Thy-1.2-/6C3-/mGFP-/CD200+/CD105-) (bottom row) in microdissected suture mesenchyme of WT and Twist1Ctsk mice at P14. Data shows significant decrease in CTSK+ mGFP cells (****$P < 0.0001$; top), CTSK+CSCs (**$P = 0.0038$; middle) and significant increase in CTSK- CSCs (**$P = 0.0093$; bottom) in Twist1Ctsk mice. WT, n=8; Twist1Ctsk, n=8, Mean ± s.d., unpaired, two-tailed Student's t test. e, Immunostaining for COMP (magenta, top row) and Alcian Blue staining (bottom row) of the LAM suture in WT and Twist1Ctsk mice at P14. Far-right, enlarged view of the yellow dotted box in each panel. Scale bars, 100 μm and 200 μm. f, Representative FACS plots (i), quantification of total CTSK+ cells (ii) and fluorescent images of CTSK+ cells (iii) from the suture of iDTRCtsk;mTmG mice after DT administration. Green, CTSK+ mGFP cells; Red, CTSK- tdTomato cells; Blue, DAPI. Scale bars, 100 μm. Significant drop in total CTSK+ cells after DT administration (***$P = 0.0004$). PBS, n=4; DT, n=3. Mean ± s.d., unpaired, two-tailed Student's t test. g, μCT images of the skull of iDTR and iDTRCtsk mice at P35 after DT administration (iDTR, n=5; iDTRCtsk, n=6). Red arrows indicate the fusing and fused sutures. h, H&E histology of the sutures of iDTR and iDTRCtsk mice after DT administration. Scale bars, 100 μm. i, FACS analysis of CTSK-negative CSCs (CTSK- CSCs) from iDTRCtsk mice with vehicle or DT. Data shows significant increase in CTSK- CSCs (**$P = 0.0079$). Mean ± s.d., unpaired two-tailed Student's t test. Scale bars in all μCT images denote 1.0 mm. Images in a-c, e, f (iii), and h represent results from at least 6 biological replicates.
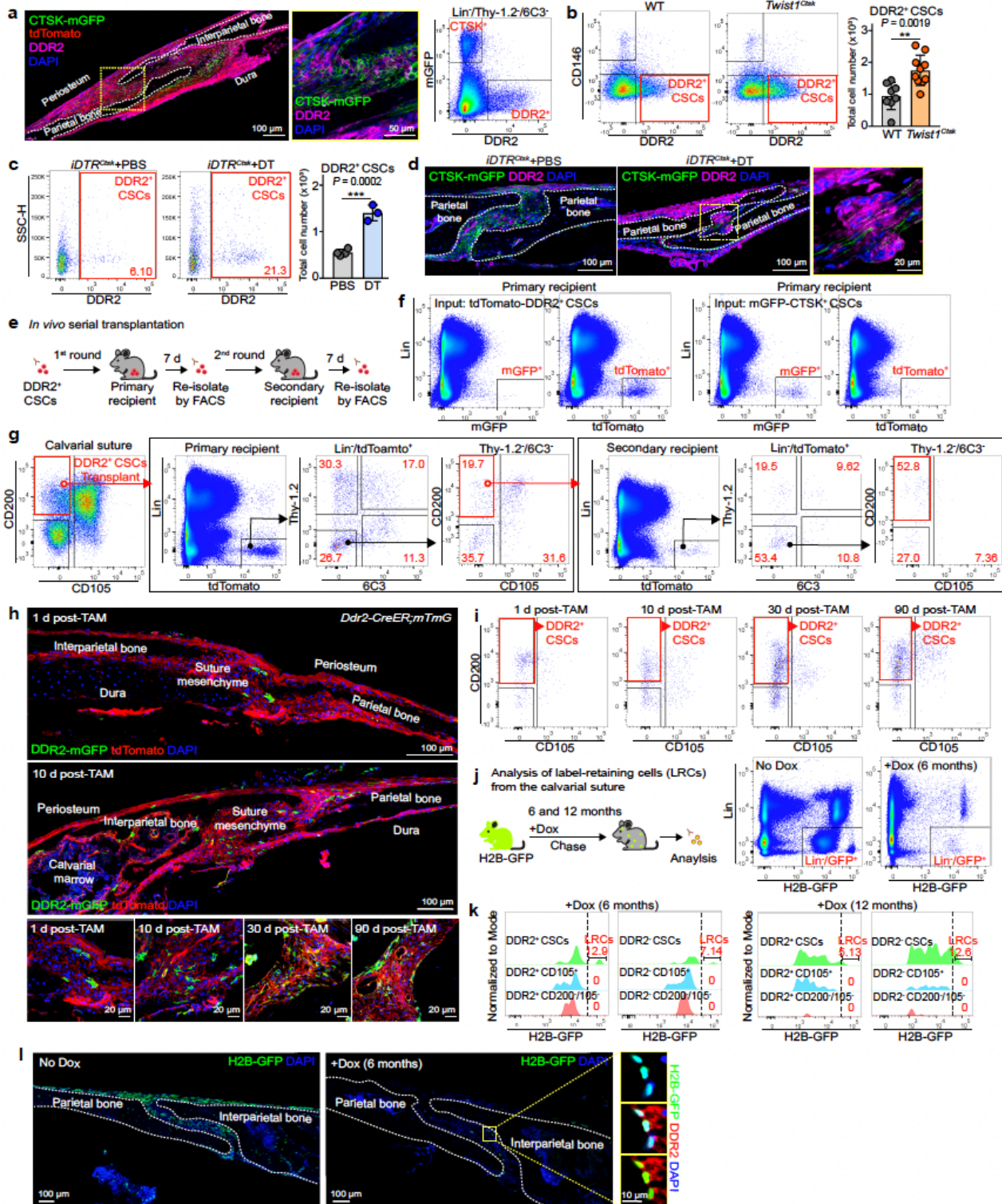
Figure 2

Figure 2

Identification of a sutural DDR2+ CSC. a, Immunostaining (left two panels) and FACS (right panel) showing sutural DDR2+ cells in Ctsk-Cre;mTmG mice at P7. Green, CTSK+ mGFP cells; Red, CTSK-tdTomato cells; Magenta, DDR2; Blue, DAPI. Right, enlarged view of the yellow dotted box. Scale bars, 100 μm and 50 μm. b, c, FACS plots and quantitative analysis demonstrating the distribution of DDR2+ CSCs (Lin-/6C3-/Thy-1.2-/mGFP-/CD200+/CD105-/DDR2+) in the suture of WT (n=8), Twist1Ctsk (n=10) (b),

and iDTRCtsk mice administered PBS (n=4) or DT (n=3) (c). Significant increase in DDR2+ CSCs (**P = 0.0019) in Twist1Ctsk mice (b) and iDTRCtsk mice (***P = 0.0002) administered with DT (c). Mean ± s.d., unpaired two-tailed Student's t test. d, Immunostaining for DDR2 in the suture of iDTRCtsk mice after vehicle or DT treatment. Green, CTSK+ mGFP cells; Magenta, DDR2; Blue, DAPI. Right, enlarged view of the yellow dotted box. Scale bars, 100 μm and 20 μm. e, A schematic representation of in vivo intramuscular serial transplantation model. f, FACS plots showing no interconversion between tdTomato-expressing DDR2+ CSCs and mGFP-expressing CTSK+ CSCs after the first round of transplantation. g, Representative FACS profiles showing the cell types derived from DDR2+ CSCs after serial transplantation. Black arrows indicate parent/daughter gates. Red boxes indicate DDR2+ CSCs. Experiments were repeated 3 independent times. h, Lineage tracing analysis of sutural DDR2+ cells using Ddr2-CreER;mTmG mice. Green, DDR2+ mGFP cells; Red, DDR2- tdTomato cells; Blue, DAPI. Scale bars, 100 μm and 20 μm. i, FACS analysis for pulse-chase labeling of DDR2+ CSCs. Red boxes indicate DDR2+ CSCs (1 d, n=7; 10 d, n=7; 30 d, n=4; 90 d, n=5). j, Long-term H2B-GFP label-retention system for slow-cycling calvarial stem cells. FACS plots showing total label-retaining cells (LRCs) after 6 months of chase post-doxycycline (Dox) administration. k, Histograms showing signal intensities of GFP fluorescence within Lin-/Thy-1.2-/6C3-/DDR2+ or DDR2- populations as determined by flow cytometry after 6 (n=9) or 12 months (n=8) of chase. LRCs were determined by the retention of high H2B-GFP signal intensity. l, Representative images of the calvarial suture in H2B-GFP mice after 6 months of chase, with DDR2 immunostaining. Green, H2B-GFP; Red, DDR2; Blue, DAPI. Scale bars, 100 and 10 μm. Images in a, d, h, and l are representative of at least 3 independent experiments.
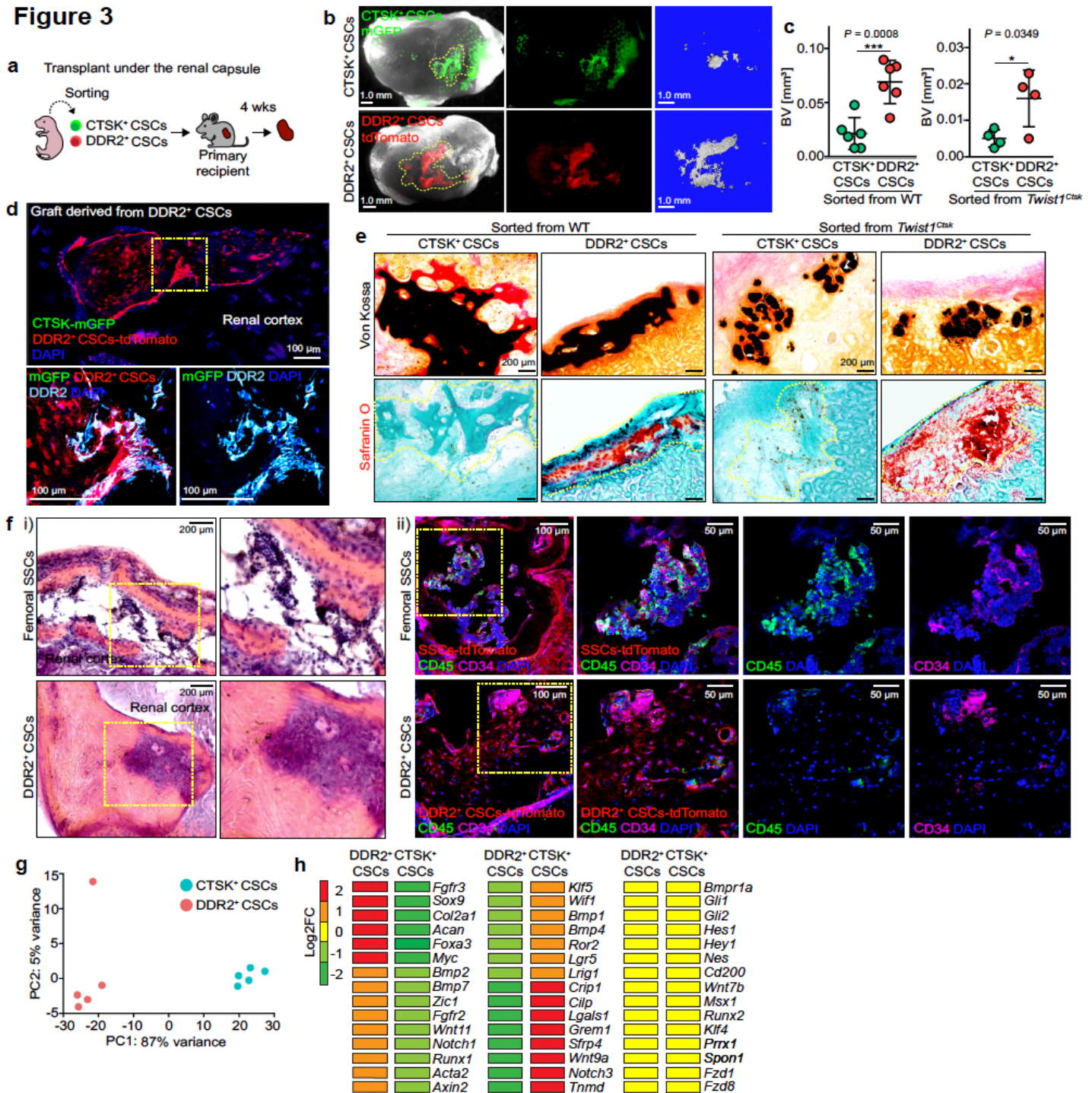
Figure 3

Endochondral-specialized DDR2+ CSCs. a, Experimental scheme for in vivo renal capsule transplantation. b, Visualization of mGFP (for CTSK+ CSCs) (top) and tdTomato (for DDR2+ CSCs)-expressing grafts (bottom) in the renal capsule at 4 weeks post-transplantation. Mineralized bone organoids were imaged by μCT scans. Scale bars, 1.0 mm. c, Quantification of bone volume (BV) when equal numbers of CTSK+ CSCs and DDR2+ CSCs were isolated from the suture of WT and Twist1Ctsk mice 4 weeks after transplantation. Mean ± s.d., unpaired, two-tailed Student's t test. d, Cryo-sectioned grafts derived from sorted DDR2+ CSCs stained with a purified DDR2 antibody. Green, CTSK+ mGFP; Red, tdTomato-

expressing graft (DDR2+ CSCs); Cyan, DDR2 antibody; Blue, DAPI. Bottom, enlarged view of the yellow dotted box. Scale bars, 100 μm. e, Representative images of Von Kossa staining (top, black) for mineralized bone and Safranin O staining (bottom, red) for cartilage in renal capsule bone organoids derived from CTSK+ CSC and DDR2+ CSC populations isolated from WT and Twist1Ctsk mice 4 weeks after transplantation. Scale bars, 200 μm. f, i) Representative H&E images from the primary grafts derived from either SSCs isolated from mouse femurs (top row) or DDR2+ CSCs (bottom row). ii) Immunostaining for CD45 (green) and CD34 (magenta) from the primary grafts (red) derived from either SSCs (top row) or DDR2+ CSCs (bottom row) 4 weeks after transplantation. Scale bars, 200, 100, and 50 μm. g, Principal component analysis (PCA) of the CTSK+ CSC and DDR2+ CSC transcriptome profiling by RNA-seq after isolation from the calvarial suture at P7. h, Heatmap of gene expression in CTSK+ CSCs and DDR2+ CSCs. Images in b, d-f are representative of 3 (e) and 5 (b, d, and f) independent experiments.
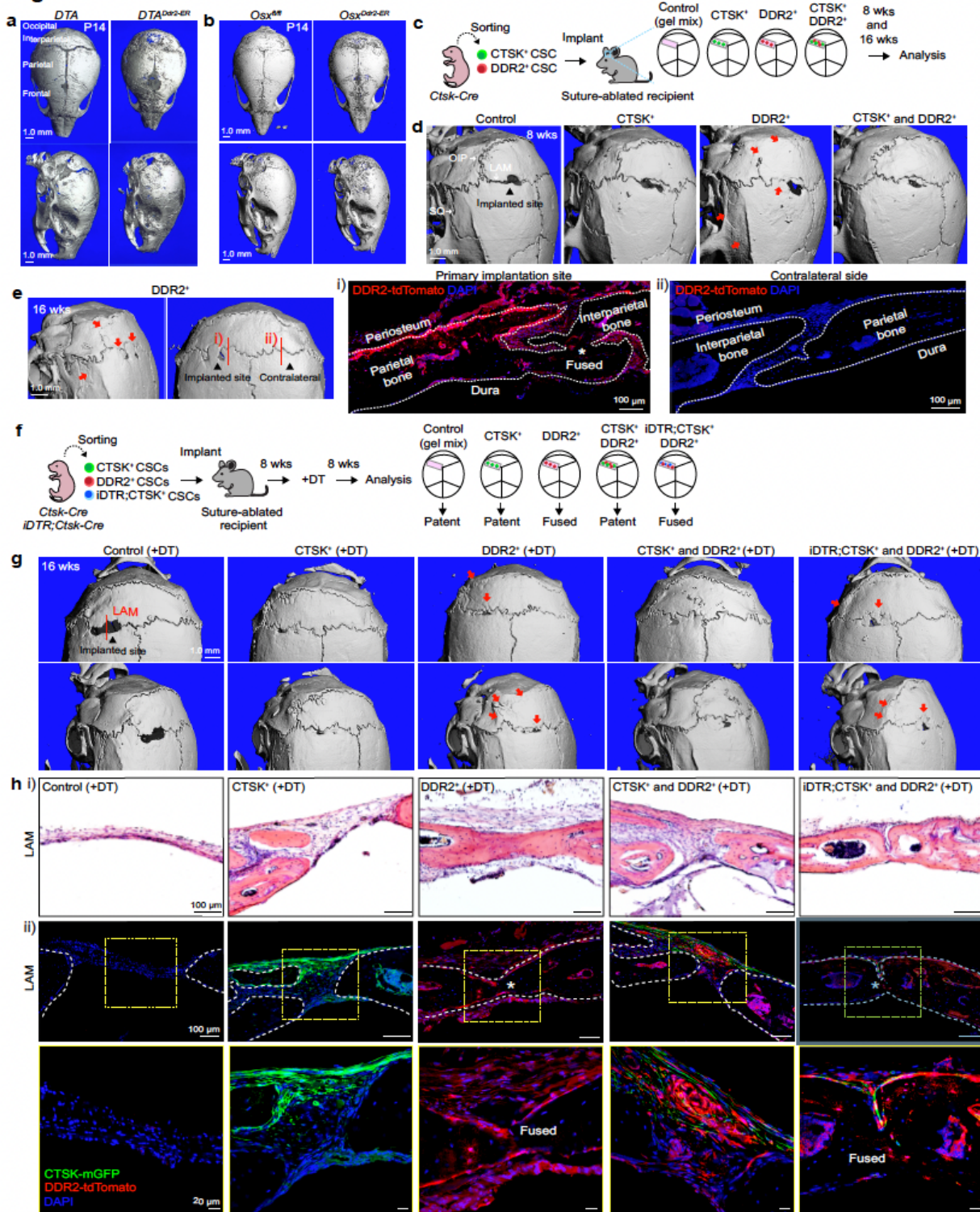
Figure 4

Figure 4

DDR2+ CSCs contribute to calvarial mineralization and suture fusion. a, b, μCT images of the skull of DTA, DTADdr2-ER (a) and Osxfl/fl, Osx Ddr2-ER (b) mice at P14, 7 days after initiating TAM administration (DTA, n=5; DTADdr2-ER, n=6; Osxfl/fl, n=7; Osx Ddr2-ER, n=6). Major skull vault bones including the frontal, parietal, interparietal, and occipital bones were indicated in the dorsal view of DTA mouse. c, Experimental scheme for orthotopic transplantation of FACS-purified CTSK+ CSCs and DDR2+

CSCs into 4-week-old suture-ablated mice. Gel mixtures (gel mix) without cells were used as a control. d, Representative µCT images of the skull at 8 weeks post-transplantation. A black arrowhead indicates the primary implantation site. Red arrows indicate the fusing and fused sutures. e, µCT images of the skull from mice 16 weeks after implantation of DDR2+ CSCs. tdTomato visualization shows engrafted DDR2+ CSCs and fusion at the primary implantation site (i), but not the contralateral side (ii). Scale bars, 100 µm. f, Experimental design and outcome of ablation of CTSK+ CSCs after transplantation. CTSK+ CSCs and iDTR;CTSK+ CSCs were isolated from P7-10 Ctsk-Cre;mTmG or iDTRCtsk;mTmG mice, respectively. All recipients were administered DT at 8 weeks post-transplantation. g, µCT images of the skull at 16 weeks post-transplantation. Red arrows indicate the fusing and fused sutures (Control, n=6; CTSK+, n=6; DDR2+, n=5; CTSK+ and DDR2+, n=5; iDTR;CTSK+ and DDR2+, n=4). h, H&E staining (i) and fluorescent imaging (ii) of the primary implantation site 16 weeks post-transplantation and DT administration. Asterisks show the region of fusion. Bottom images, enlarged view of the yellow dotted box. Green, CTSK+ mGFP cells; Red, DDR2+ tdTomato cells; Blue, DAPI. Scale bars, 100 µm and 20 µm. Scale bars in all µCT images denote 1.0 mm. Images in e and h are representative of 3 independent experiments.
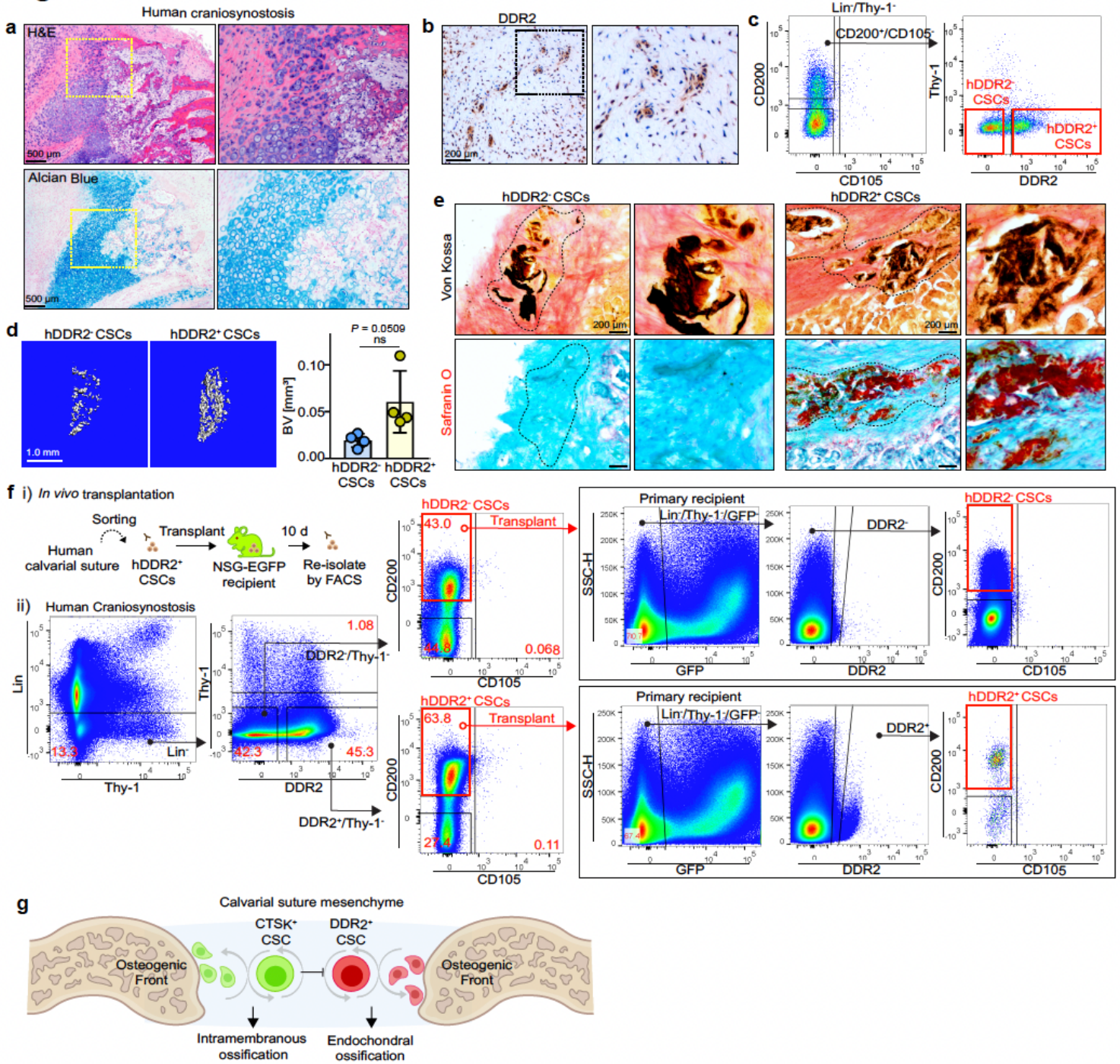
Figure 5

Figure 5

Identification of human DDR2+ CSCs. a, Histological analysis using H&E (n=14) (top) and Alcian Blue (n=7) (bottom) staining of calvarial specimens from patients with craniosynostosis. Scale bars, 500 μm. b, Immunohistochemistry for DDR2 in calvarial specimens from patients with craniosynostosis (n=7). Scale bars, 200 μm. c, FACS analysis of hDDR2+ and hDDR2- CSCs in the calvarium of patients with craniosynostosis. Lin indicates CD31, CD45, and CD235a. d, μCT scans (left two panels) and bone volume (BV) quantification (right panel) of bone organoids derived from hDDR2+ and hDDR2- CSCs. Scale bars, 1.0 mm. P = non-significant or ns., Mean ± s.d., unpaired, two-tailed Student's t test. e,

Representative images of Von Kossa staining (black; top row) for mineralized bone and Safranin O staining (red; bottom row) for cartilage in the renal capsule bone organoids derived from hDDR2- and hDDR2+ CSCs at 4 weeks post-transplantation. Scale bars, 200 μm. f, (i) A schematic representation of in vivo characterization of hDDR2- and hDDR2+ CSCs. (ii) FACS plots showing the self-renewal and differentiation capacity of hDDR2+ and hDDR2- CSCs. Lin indicates CD31, CD45, and CD235a. g, A graphical model of the role of DDR2+ CSCs and CTSK+ CSCs in the calvarial suture. FACS plots are representative of 3 (f) or 10 (c) independent experiments. Images in a, b, and e are representative of at least 3 independent experiments.

Supplementary Files

This is a list of supplementary files associated with this preprint. Click to download.

- BokCalvarialExtendedData.pdf